

Infrared and Raman line shapes for ice Ih. II. H₂O and D₂O

Cite as: J. Chem. Phys. **133**, 244504 (2010); <https://doi.org/10.1063/1.3516460>

Submitted: 07 September 2010 . Accepted: 26 October 2010 . Published Online: 28 December 2010

F. Li, and J. L. Skinner



View Online



Export Citation

ARTICLES YOU MAY BE INTERESTED IN

[Infrared and Raman line shapes for ice Ih. I. Dilute HOD in H₂O and D₂O](#)

The Journal of Chemical Physics **132**, 204505 (2010); <https://doi.org/10.1063/1.3430518>

[IR and Raman spectra of liquid water: Theory and interpretation](#)

The Journal of Chemical Physics **128**, 224511 (2008); <https://doi.org/10.1063/1.2925258>

[Raman intensities of single crystal ice I_h](#)

The Journal of Chemical Physics **67**, 4794 (1977); <https://doi.org/10.1063/1.434683>

Infrared and Raman line shapes for ice Ih. II. H_2O and D_2O F. Li and J. L. Skinner^{a)}*Theoretical Chemistry Institute and Department of Chemistry, University of Wisconsin, Madison, Wisconsin 53706, USA*

(Received 7 September 2010; accepted 26 October 2010; published online 28 December 2010)

We present a theoretical study of infrared and Raman line shapes of polycrystalline and single crystal ice Ih, for both water and heavy water, at 1, 125, and 245 K. Our calculations involve a mixed quantum/classical approach, a new water simulation model with explicit three-body interactions, transition frequency and dipole maps, and intramolecular and intermolecular vibrational coupling maps. Our theoretical spectra are in reasonable agreement with experimental spectra (available only near the two higher temperatures). We trace the origins of the different spectral peaks to weak and strong intermolecular couplings. We also discuss the delocalization of the vibrational eigenstates in terms of the competing effects of disorder and coupling. © 2010 American Institute of Physics. [doi:10.1063/1.3516460]

I. INTRODUCTION

Understanding the structure and dynamics of ice Ih has been the objective of numerous studies.^{1–12} Since OH stretch frequencies of the water molecule are very sensitive to molecular environments,¹³ infrared (IR) and Raman line shapes in the OH stretch region of ice Ih have been measured and studied for 50 years.^{14–28} Similar experiments have also been performed on D_2O ice Ih. The spectra show interesting and complicated vibrational structure, which depends upon temperature, and in the case of Raman spectroscopy, upon incident and scattered electric field polarizations. The OH stretch local modes in the solid are coupled through intramolecular and intermolecular interactions. If ice Ih were an ordered crystal, then the vibrational eigenstates would be extended in space and would reflect the crystal symmetry. But, in fact, ice Ih is a disordered crystal with respect to the proton positions.¹ Such disorder, of course, tends to localize the vibrational eigenstates. Thus, the competing effects of vibrational coupling, proton disorder, and thermal fluctuations, make for very rich spectra, which, correspondingly, have been difficult to interpret.^{19,29–36}

As a first step³⁷ in the calculation and interpretation of these spectra, we have considered the simpler systems of dilute HOD in H_2O or D_2O ice Ih.^{14,16,20,22,23} In these instances, the OD or OH vibrational chromophore, respectively, is off resonance and, therefore, to a large extent uncoupled, from the other stretches. The IR and Raman line shapes are considerably simpler, with a single main peak corresponding to the fundamental OD or OH stretch. The positions and widths of the peak depend on temperature. We found³⁷ that the line widths arise from a combination of static inhomogeneous broadening due to the (essentially quenched) proton disorder, and thermal broadening (but which is substantially motionally narrowed) due to low-frequency lattice vibrations. These line shapes are much narrower than the correspond-

ing line shapes in liquid H_2O or D_2O because the liquid is more disordered still (and so it has a broader frequency distribution), and because motional narrowing occurs to a much smaller extent in the liquid. In addition, the ice line shapes are considerably red-shifted from those in the liquid, due to stronger and more complete hydrogen bonding. Finally, we assigned a weak shoulder on the blue side of the Raman spectra as arising from a combination band with the intermolecular hydrogen-bond stretch, which is consistent with previous interpretation.²⁰

Armed with this understanding of the spectroscopy of the local chromophores and the general validation (from the successful comparison with experiment) of our theoretical approaches, in this paper we now consider the IR and Raman spectra of H_2O and D_2O ice Ih. A thorough discussion of the theoretical literature for this problem was presented in our earlier paper,³⁷ and so we do not repeat this here. We do simply note that several previous studies have treated all of the nuclear degrees of freedom classically.^{38–43} Herein, however, we pursue a mixed quantum/classical approach, where all the OH (OD) stretch degrees of freedom are treated quantum mechanically, while the remaining nuclear degrees of freedom (the bath) are treated classically.^{44–48} Specifically, we build to a large extent on the theoretical study of the isotopically dilute system in ice,³⁷ which in turn built on related studies of liquid water.^{45,47} This approach uses electronic structure-based maps, wherein the transition frequency and dipole are related to local electric fields. For the fully coupled systems of H_2O and D_2O , we need to supplement these maps with maps for the intramolecular and intermolecular vibrational coupling,⁴⁷ which we develop herein.

As in our previous paper, we use the newly developed E3B simulation model for liquid water.⁴⁹ This choice is motivated by the desire to use a model that freezes close to the experimental melting point of water. Moreover, the model has the geometry and interaction-site charges of the popular TIP4P model,⁵⁰ which has two consequences: we can use the TIP4P model to develop the required maps, and these maps should be useful with any other model that has the

^{a)} Author to whom correspondence should be addressed. Electronic mail: skinner@chem.wisc.edu.

same geometry and charges. As in our previous paper with the isotopes,³⁷ in which we first verified that the maps, with the E3B model, worked well for the IR and Raman spectra for liquid water, herein we first show that for fully coupled H₂O and D₂O we can obtain reasonable agreement with experimental IR and Raman line shapes for liquid H₂O and D₂O. For H₂O, we earlier had obtained similar results using the SPC/E (simple point charge/extended) simulation model and the appropriate maps.^{47,51} Theoretical results for liquid D₂O are shown here for the first time. We then go on to calculate IR and Raman line shapes for polycrystalline and single crystal H₂O and D₂O ice Ih. Our results are in reasonable agreement with experiment. We identify the origins of the different peaks by examining the spectra at very low temperature (1 K) and separately considering the effects of weak and strong intermolecular couplings, and also discuss the delocalization of the vibrational eigenstates in terms of the competing effects of diagonal and off-diagonal disorder, as produced by the proton disorder in ice Ih, and vibrational coupling.

II. LINE SHAPE CALCULATIONS

A. Mixed quantum/classical formalism and ES/MD approach

Both IR and Raman line shapes can be written in terms of quantum time-correlation functions. In the case of IR, if the electric field of the excitation light is polarized in the \hat{p} direction, the linear absorption line shape is (Ref. 52)

$$I_p(\omega) \propto \text{Re} \int_0^\infty dt e^{i\omega t} \langle \hat{p} \cdot \vec{\mu}(t) \vec{\mu}(0) \cdot \hat{p} \rangle, \quad (1)$$

where $\vec{\mu}(t)$ is the Heisenberg expression for the dipole operator of the system at time t and the brackets indicate a quantum equilibrium statistical mechanical average. For an isotropic system, this result is independent of \hat{p} . For an oriented single crystal, however, the results do depend on the polarization direction \hat{p} . For ice Ih, the set of orthogonal unit vectors are denoted by a , a' , and c , and crystal symmetry shows that $I_a = I_{a'}$.

In the Raman case, the incident beam is polarized in a particular direction, call it \hat{p} , and the scattered beam is polarized in direction \hat{q} . Similar to the IR line shape, the Raman line shape can be written as (Ref. 52)

$$I_{pq}(\omega) \propto \text{Re} \int_0^\infty dt e^{i\omega t} \langle \hat{p} \cdot \underline{\alpha}(t) \cdot \hat{q} \hat{p} \cdot \underline{\alpha}(0) \cdot \hat{q} \rangle, \quad (2)$$

where $\underline{\alpha}$ is the polarizability tensor operator for the system. Thus, in general, there are six different line shapes: I_{cc} , I_{aa} , $I_{a'a'}$, I_{ca} , $I_{ca'}$, and $I_{aa'}$. Considering the symmetry of the hexagonal lattice, however, the six line shapes reduce to two independent parallel-polarized (I_{cc} and I_{aa}) and two independent perpendicular-polarized (I_{ca} and $I_{aa'}$) intensities.

Within the mixed quantum/classical approach, for a system of coupled chromophores the IR line shapes can be written as (Ref. 47)

$$I_p(\omega) \propto \text{Re} \int_0^\infty dt e^{i\omega t} \sum_{ij} \langle m_{ip}(t) F_{ij}(t) m_{jp}(0) \rangle e^{-t/2T_1}, \quad (3)$$

TABLE I. Maps for the transition frequencies, matrix elements, dipole derivative, and intramolecular coupling. Frequencies are in cm^{-1} and all other quantities are in atomic units.

$\omega_{\text{OH}} = 3732.9 - 3519.8E - 1.5352 \times 10^5 E^2$
$\omega_{\text{OD}} = 2748.2 - 2572.2E - 1.0298 \times 10^5 E^2$
$x_{\text{OH}} = 0.19318 - 1.7248 \times 10^{-5} \omega_{\text{OH}}$
$x_{\text{OD}} = 0.16598 - 2.0752 \times 10^{-5} \omega_{\text{OD}}$
$p_{\text{OH}} = 1.6102 + 5.8697 \times 10^{-4} \omega_{\text{OH}}$
$p_{\text{OD}} = 1.9813 + 9.1419 \times 10^{-4} \omega_{\text{OD}}$
$\mu' = 0.1622 + 10.381E + 137.6E^2$
$k_{ij}^a = -0.0062003 + 0.1238(E_i + E_j)$

where $m_{ip}(t)$ is the laboratory-fixed component p at time t of the transition dipole for chromophore i . This form follows from writing the dipole operator as a sum of operators for each local-mode chromophore. Here, $F_{ij}(t)$ are the elements of the matrix $F(t)$, which satisfies the equation,

$$\dot{F}(t) = -iF(t)\kappa(t), \quad (4)$$

subject to the initial condition that $F_{ij}(0) = \delta_{ij}$, and with

$$\kappa_{ij}(t) = \omega_i(t)\delta_{ij} + \omega_{ij}(t)(1 - \delta_{ij}). \quad (5)$$

Thus, $\kappa(t)$ is a matrix whose diagonal elements are the fluctuating transition frequencies, $\omega_i(t)$ and whose off-diagonal elements are the fluctuating coupling elements, $\omega_{ij}(t)$. The angular brackets now denote a classical equilibrium statistical mechanical average. Within this approach, the effects of the lifetime of an OH stretch excitation in water, T_1 , must be included phenomenologically, as shown; the value for T_1 will be taken from experiments. The formulas for the Raman line shapes are similarly

$$I_{pq}(\omega) \propto \text{Re} \int_0^\infty dt e^{i\omega t} \sum_{ij} \langle a_{ipq}(t) F_{ij}(t) a_{jpq}(0) \rangle e^{-t/2T_1}, \quad (6)$$

where $a_{ipq}(t)$ is the pq component at time t of the transition polarizability for chromophore i .

In order to implement these formulae, one needs to be able to determine, from a classical molecular dynamics (MD) simulation of the bath variables, the fluctuating transition frequencies, transition dipoles, transition polarizabilities, and vibrational couplings. We describe our maps to determine these quantities below. Since these latter quantities come from electronic structure (ES) calculations, we call this the ES/MD approach.⁴⁴

B. Transition frequencies, dipoles, and polarizabilities

In our previous paper³⁷ on the dilute HOD isotopes, we described in detail our procedure for determining maps for individual OH and OD stretch chromophores. The basic idea is to perform ES calculations on water clusters, taken from a TIP4P simulation of liquid water, to determine reasonably accurate transition frequencies and dipoles for solvated chromophores, and then relate these quantities to local electric fields. The OH and OD stretch frequencies are determined by maps that are quadratic in the local electric field,³⁷ as shown in Table I. In the bond-dipole approximation, the projection

of the transition dipole moment on the laboratory-fixed p axis is approximately given by⁴⁷

$$m_p = \mu' x \hat{u} \cdot \hat{p}, \quad (7)$$

where μ' is the magnitude of the dipole derivative, x is the 0–1 matrix element of the OH (OD) stretch coordinate, and \hat{u} is the unit vector in the OH (OD) direction. Here, μ' is given by a quadratic function of the local electric field and x is related linearly to the transition frequency,³⁷ as shown in Table I. In the bond-polarizability model, the pq matrix element of the transition polarizability for an individual chromophore is given by⁴⁷

$$a_{pq} = (\alpha'_{\parallel} - \alpha'_{\perp})x \hat{p} \cdot \hat{u} \hat{u} \cdot \hat{q} + \alpha'_{\perp}x \hat{p} \cdot \hat{q}, \quad (8)$$

where α'_{\parallel} and α'_{\perp} are constants, whose ratio $\alpha'_{\parallel}/\alpha'_{\perp} = 5.6$.³⁷

C. Intramolecular coupling

Both the intramolecular and intermolecular couplings are determined using the strategy developed by Auer and Skinner in their study of the vibrational spectra of liquid water.⁴⁷ In the local-mode basis, to lowest order the coupling frequency ω_{ij} between the two OH stretches on the same molecules is (Ref. 53)

$$\hbar\omega_{ij} = \frac{k_{ij}^a x_i x_j + \cos(\phi) p_i p_j}{m_O}, \quad (9)$$

where k_{ij}^a is the second derivative of the potential energy with respect to both bond lengths, evaluated at the minimum, x_i is the position matrix element discussed above for chromophore i , p_i is the corresponding 0–1 momentum matrix element, ϕ is the HOH bond angle, and m_O is the oxygen mass. The momentum coupling arises from the transformation from cartesian to internal coordinates.

Following the ES/MD approach originally developed by Corcelli *et al.*⁴⁴ and Auer *et al.*⁴⁵ on SPC/E water model, and most recently implemented by Li and Skinner³⁷ for the TIP4P water model, approximately 100 clusters are generated from an MD simulation of TIP4P water at 300 K to determine k_{ij}^a . These “oxygen-centered” clusters were generated by choosing an oxygen randomly in the simulation and including in the cluster any water with an oxygen within 4.07 Å of the center oxygen. This distance was chosen to give approximately the same number of waters in these clusters as in the “hydrogen-centered” clusters used for other maps.³⁷ Once again point charges were included up to a cutoff of 7.831 Å. The two bonds of the central water were minimized keeping the center of mass fixed. An analytic second derivative calculation was performed at this geometry to obtain k_{ij}^a . Our strategy⁴⁷ is to relate k_{ij}^a to the electric fields on the hydrogen atoms of the molecule of interest. We find that in this case k_{ij}^a is given quite well by a formula that is linear in the sum of these two fields, as shown in Table I and Fig. 1.

The momentum matrix elements are easily found using the same discrete variable representation scheme as for x ,^{37,54,55} and the results can also be linearly related to the transition frequency, as described in Table I. The HOH bond angle in TIP4P, as determined from gas-phase experiment,

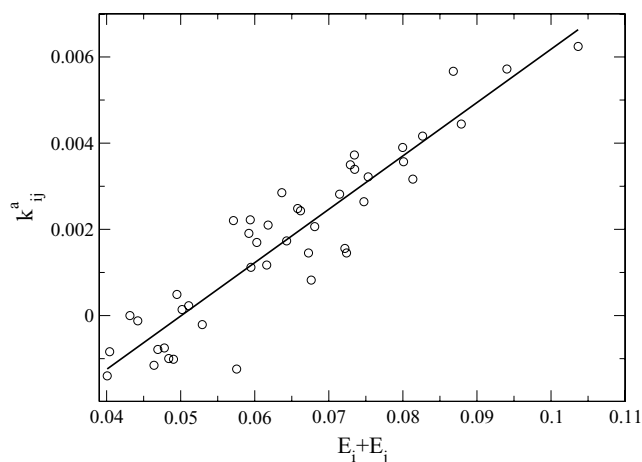


FIG. 1. Intramolecular coupling k_{ij}^a [in atomic units (a.u.)] vs the electric field sum $E_i + E_j$ (in a.u.). The solid line is the best linear fit.

is 104.52°. These, together with the position matrix elements, now allow us to determine ω_{ij} for chromophores located on the same molecule. Using this result, we can approximate the value in the gas phase by taking the electric fields $E_i = E_j = 0$ and setting x_i , p_i to the gas-phase values. This gives -43.7 cm^{-1} for H_2O and -46.0 cm^{-1} for D_2O , which are close to the values of about -49.4 cm^{-1} (for H_2O) and -59.3 cm^{-1} (for D_2O), as inferred from the experimental gas-phase splittings between symmetric and antisymmetric stretch vibrations.^{56,57} Note that for gas-phase water both terms in the intramolecular coupling are negative and the momentum term dominates. The position matrix elements are smaller for OD, and the momentum matrix elements are larger, leading to a larger (in magnitude) intramolecular coupling in D_2O .

D. Intermolecular coupling

For the vibrational coupling between OH stretch chromophores on different molecules, the simplest assumption is that of transition dipole interactions.^{37,47,58,59} In this case, the coupling frequency is given by

$$\hbar\omega_{ij} = k_{ij}^e x_i x_j, \quad (10)$$

where x_i is the same matrix element as before and k_{ij}^e is given by

$$k_{ij}^e = \frac{\mu'_i \mu'_j \{ \hat{u}_i \cdot \hat{u}_j - 3[(\hat{u}_i \cdot \hat{n}_{ij})(\hat{u}_j \cdot \hat{n}_{ij})] \}}{r_{ij}^3}, \quad (11)$$

where \hat{n}_{ij} is a unit vector along the line connecting the dipoles and r_{ij} is the distance between the dipoles. A question arises: where along each OH bond should one place the transition dipole? A number of different positions have been suggested;^{47,59} here we again turn to comparison with *ab initio* calculations to guide us. Following Auer and Skinner,⁴⁷ we generate a number of dimer-centered clusters and determine k_{ij}^e for pairs of OH bonds on the dimer. Assuming the transition-dipole coupling model, we then determine the best-fit position of the dipole—we find that it is along the OH bond 0.67 Å from the oxygen atom. Note that in each dimer we generated, there are two “strong” couplings,

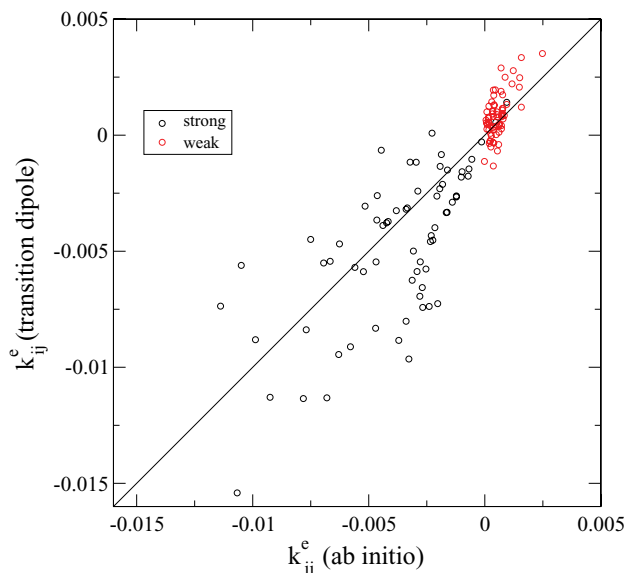


FIG. 2. Calculated (*ab initio*) intermolecular coupling k_{ij}^e (in a.u.) vs transition dipole approximation. The line simply indicates the diagonal.

between the hydrogen-bonded donor OH and the OH bonds on the acceptor molecule, and two “weak” couplings involving the other OH on the donor molecule. In Fig. 2, we plot the *ab initio* coupling versus the transition dipole approximation to it. The strong couplings are in black and the weak couplings are in red. Despite the scatter, this is probably an acceptable approximation and it captures the basic feature that the strong couplings are generally negative and weak couplings are generally positive, which is due to the orientations of the different types of OH pairs.

III. LINE SHAPE RESULTS

A. IR and Raman line shapes for liquid water

We have previously calculated IR and Raman line shapes for liquid water using the same approach but with a different (SPC/E) water simulation model.^{47,51} Thus, here we first ascertain that we can obtain similarly good results using the E3B model,⁴⁹ with these TIP4P-based maps, as discussed in Introduction.

An MD simulation of liquid H₂O within the E3B model was performed using the NVE (constant number of particles, volume, and energy) ensemble with 128 molecules at the experimental density at 300 K using the suitably modified GROMACS package 3.3.⁶⁰ Periodic boundary conditions were employed, and electrostatic forces were computed using the particle-mesh Ewald technique.^{61,62} The equations of motion were integrated with the leapfrog algorithm, using the SETTLE scheme with a 1 fs time step.⁶³ For H₂O spectra, at every 10 fs in the simulation, at each H atom the electric field from point charges on waters within the cutoff is computed. From this, one obtains the local-mode frequencies, ω_i . From these frequencies, one obtains the matrix elements x_i and p_i , which, together with the electric fields and the atomic positions, allows one to obtain the intramolecular coupling frequencies and $a_{ipq}(t)$. Similarly, at every 10 fs, one can calcu-

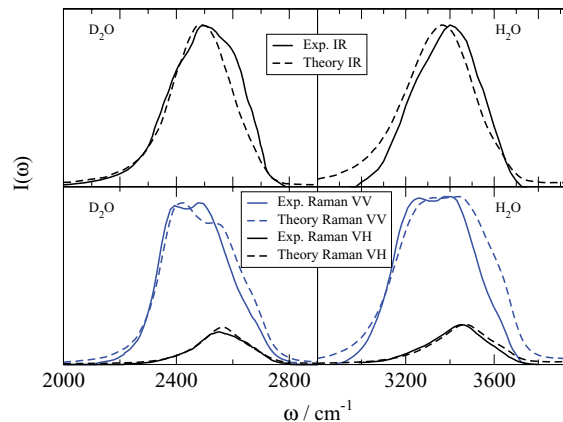


FIG. 3. Top panels: Theoretical (dashed line) and experimental (Refs. 65 and 67) (solid line) IR line shape for liquid H₂O (right) and D₂O (left). Theory line shape is at 300 K, and experimental line shapes are at 298 K. Bottom panels: Theoretical (dashed line) and experimental (Ref. 66) (solid line) Raman VH and VV line shapes for liquid H₂O (right) and D₂O (left). Theoretical line shapes are at 300 K. Experimental line shapes are at 303 K.

late the dipole derivative μ'_i , which then leads to $m_{ip}(t)$ and the intermolecular coupling frequencies. A similar simulation was performed for D₂O, using the same potential but with the appropriate deuterium mass and the experimental D₂O density.

The calculated IR and polarized (VV) and depolarized (VH) Raman spectra for H₂O at 300 K are shown in Fig. 3 (right two panels, dashed lines). Note that for this calculation we used the lifetime of 260 fs.⁶⁴ Also shown are experimental results^{65,66} at 298 K (IR) and 303 K (Raman). For the IR spectra, the theoretical and experimental spectra are normalized to have the same peak height. Similarly, the theoretical and experimental Raman VV spectra are normalized to have the same peak height; however, for both theory and experiment the relative intensities of the VH and VV peaks have not been adjusted. In all aspects (line positions, shapes, widths, and relative VH and VV intensities), there is reasonably good agreement between theory and experiment. The agreement is comparable to that obtained for the SPC/E model.^{47,51} These results were interpreted in terms of vibrational coupling.^{47,51} Similar results for D₂O are shown in the left two panels of Fig. 3, with similarly good agreement between theory and experiment.^{66,67} In this case, we estimated the lifetime to be 600 fs (assuming the same ratio as for the lifetimes for the OH and OD stretch of HOD).

B. IR and Raman line shapes for ice Ih

To simulate the ice line shapes, we start with the proton-disordered configuration as discussed in our previous paper,³⁷ for 432 water molecules.⁶⁸ We then ran NVE MD simulations for H₂O and D₂O at 245 K, in each case using the experimental lattice constants at 245 K.¹ The H₂O and D₂O vibrational lifetimes in ice are taken to be 300 and 700 fs, respectively. The former was measured,²⁸ while the latter is estimated (using the same scaling as we did for HOD³⁷). If the latter is not very accurate, it does not make much difference, since the spectral widths are dominated by other mechanisms.

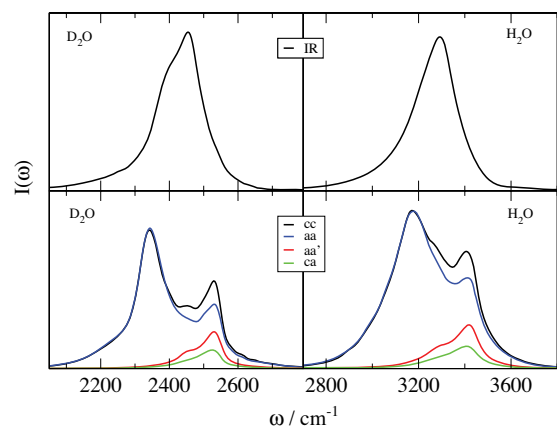


FIG. 4. Theoretical IR and Raman line shapes for polycrystalline and single crystal ice Ih, respectively, at 245 K. Top left is IR line shape for D₂O. Top right is IR line shape for H₂O. Bottom left are Raman line shapes for D₂O. Bottom right are Raman line shapes for H₂O.

The results, for D₂O (left two panels) and H₂O (right two panels), are shown in Fig. 4. The IR line shapes (top two panels) are for the polycrystalline ice Ih, where we have averaged over the three orthogonal polarizations. The Raman line shapes (bottom two panels) are for single crystal ice Ih, and we show the two polarized and two depolarized line shapes. One sees shoulders and asymmetric IR line shapes in both cases. The Raman line shapes show more structure, with the main peak lower in frequency than the IR peak, while the secondary peak is higher than the IR peak. The Raman spectra also show a weak third peak at about 2450 cm⁻¹ for D₂O and 3300 cm⁻¹ for H₂O. The dependence on polarization is profound, with significantly smaller amplitude and absence of the main peak for the depolarized intensities.

In an effort to sharpen the spectra, and in order to compare with experiments at lower temperature, we perform similar simulations but now at 125 K, which are reported in Fig. 5. The main difference between these spectra and those at the higher temperature, is that the IR line shape for D₂O now shows a peak on the red side instead of a shoulder, and the weak third peak in the Raman spectra for H₂O is now sharper.

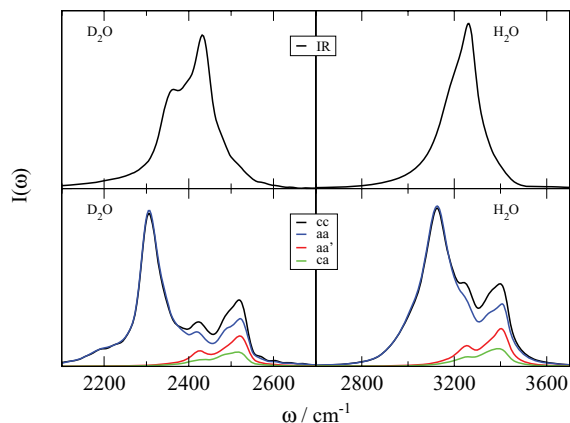


FIG. 5. Theoretical IR and Raman line shapes for polycrystalline and single crystal ice Ih, respectively, at 125 K. Top left is IR line shape for D₂O. Top right is IR line shape for H₂O. Bottom left are Raman line shapes for D₂O. Bottom right are Raman line shapes for H₂O.

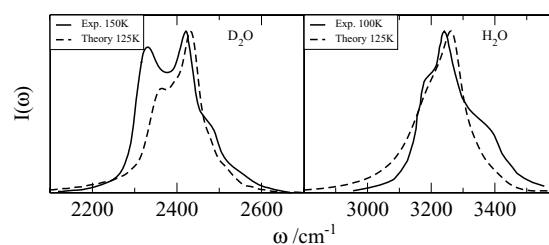


FIG. 6. Theoretical (at 125 K) and experimental (Refs. 19 and 23) IR line shapes for polycrystalline D₂O (left) and H₂O (right) ice Ih.

In Fig. 6, we compare theoretical IR spectra at 125 K, for polycrystalline D₂O and H₂O ice Ih, with experimental results^{19,23} (albeit at slightly different temperatures). The red peak in the IR spectrum for D₂O is more pronounced in experiment. In H₂O, the red and blue shoulders are both more pronounced in experiment. Overall agreement between theory and experiment is certainly not excellent but is qualitatively good.

In Fig. 7, we compare theoretical Raman spectra for single crystal D₂O and H₂O at 245 K, with experimental spectra²⁰ at slightly higher (269 K) temperature. In this case theory fares better, capturing peak frequencies and intensities very well.

IV. ANALYSIS AND DISCUSSION

Our calculated line shapes at 125 and 245 K are in reasonable agreement with experiment and show considerable structure. Our next task is to try to interpret this structure. To this end, it is helpful to calculate theoretical line shapes at even lower temperature, to suppress the contributions from thermal broadening. Theoretical IR and *aa* and *aa'* Raman line shapes for 1 K are shown in Fig. 8, for H₂O. One sees essentially five peaks, at about 3060, 3150, 3220, 3330, and 3395 cm⁻¹ (as shown by the vertical dashed lines), which are active to a greater or lesser extent in each spectrum.

To understand the origin of these peaks, we clearly have to understand the magnitudes of the intramolecular and intermolecular couplings. In Fig. 9, we show probability

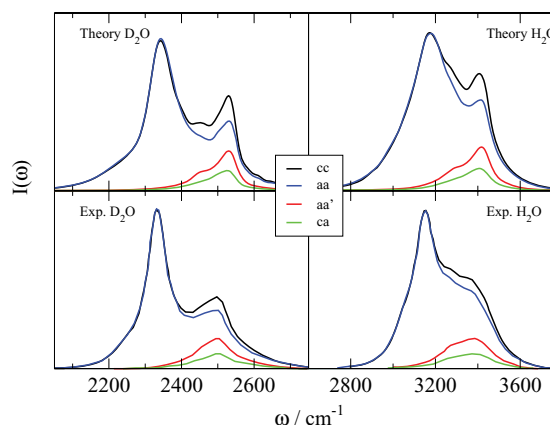


FIG. 7. Theoretical (at 245 K) and experimental (Ref. 20) Raman line shapes for single crystal D₂O and H₂O ice Ih. Top panels are theory; bottom are experiment. Left panels are for D₂O; right panels are for H₂O.

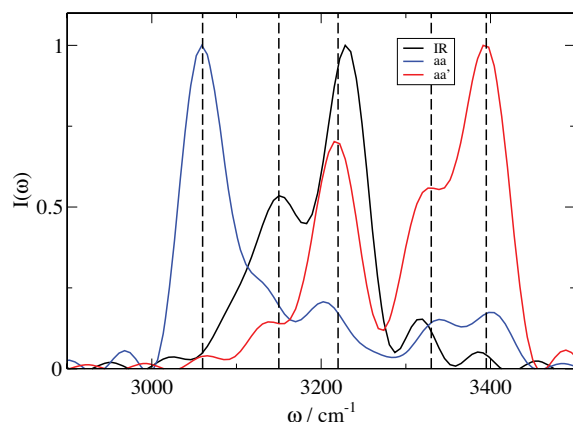


FIG. 8. Theoretical IR and selected Raman line shapes for H_2O ice Ih at 1 K. The three line shapes are peak normalized.

distributions of the intramolecular and intermolecular (nearest-neighbor only) OH stretch couplings at 1 K. The intramolecular coupling distribution peaks near zero, even though in liquid water it peaks⁴⁷ near -30 cm^{-1} . The difference comes about because the second derivative k_{ij}^a is larger in ice (because of larger electric fields), and positive, which almost cancels the negative momentum term in Eq. (9). This suggests that this intramolecular coupling will have only weak effect on the spectroscopy.

The intermolecular coupling distribution has a peak centered at about -50 cm^{-1} coming from the closest pairs of OH bonds in the ice Ih lattice, and four peaks centered at from $+2$ to $+16 \text{ cm}^{-1}$ arising from pairs of OH bonds on nearest-neighbor molecules that are somewhat farther away and with different orientations. Treating the proton disorder as locally statistical, we find that the areas of these peaks should be in the ratio of 3:2:6:1 (from left to right), in rough agreement with the figure. These different types of pairs of OH bonds are shown schematically in Fig. 10. These distributions are all shifted from their positions in liquid water due to stronger hydrogen bonding. The distribution of strong intermolecular coupling is surprisingly broad, at first glance, since the angles between each pair of the OH bonds is approximately the same. However, the proton disorder causes the dipole derivatives to be broadly distributed, which produces the relatively broad

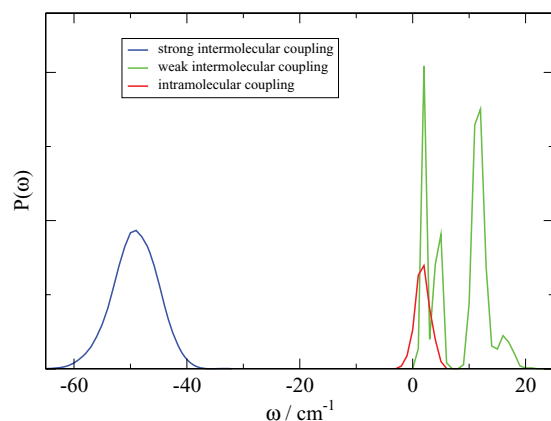


FIG. 9. Nearest-neighbor intermolecular and intramolecular coupling distributions at 1 K.

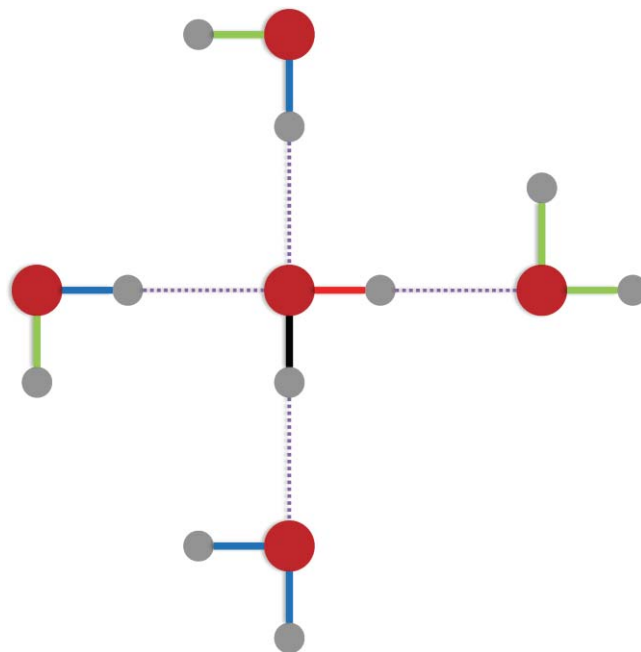


FIG. 10. A schematic representation of a water pentamer from the ice Ih lattice showing different pairs of OH bonds. The OH bond of interest is shown in black. The bond to which it is coupled through an intramolecular interaction is shown in red. The bonds to which it is coupled through “strong” intermolecular interactions are shown in blue. The bonds to which it is coupled through “weak” intermolecular interactions are shown in green. Angles are not to scale in this schematic drawing!

distribution of intermolecular coupling. Note that the magnitude of the strong intermolecular coupling is larger in ice than in liquid water because the transition dipoles are larger in ice due to stronger hydrogen bonding.⁶⁹

To understand the effect of these couplings, in Fig. 11, we show the distributions of eigenfrequencies for various circumstances. These come from simply taking snapshots from our simulation at 1 K, diagonalizing the vibrational exciton Hamiltonian, and averaging. First we show the frequency

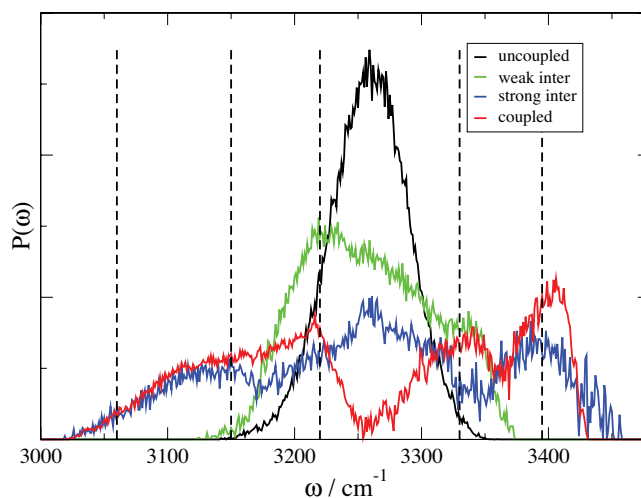


FIG. 11. Theoretical frequency distributions of H_2O ice Ih at 1 K. The black line comes from neglecting all coupling. The green line includes only the weak intermolecular coupling. The blue line includes only the strong intermolecular coupling. The red line is for the fully (intermolecular and intramolecular) coupled system.

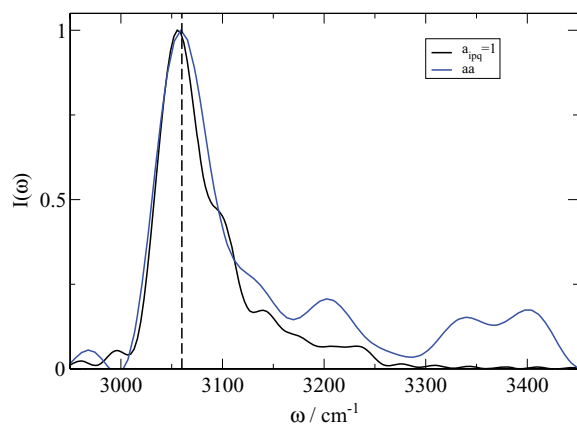


FIG. 12. Hypothetical Raman spectrum with $a_{ipq} = 1$, compared to theoretical aa Raman spectrum, both at 1 K.

distribution with all vibrational coupling set to zero. This peaks at about 3260 cm^{-1} and has a breadth due to proton disorder, as discussed in the first paper of this (two-part) series.³⁷ Next we show the frequency distribution with only the weak (and positive) intermolecular coupling included. This distribution is asymmetric, with a strong peak at about 3220 cm^{-1} , and a strong shoulder at about 3340 cm^{-1} . The extra broadening, compared to the peak for the uncoupled distribution, is consistent with the magnitude of the weak intermolecular coupling on the order of 10 cm^{-1} . Next we show the frequency distribution with only the strong (and negative) intermolecular coupling included. This distribution has three peaks, at about 3140 , 3260 , and 3390 cm^{-1} . The much larger frequency dispersion in this case is consistent with the strong intermolecular coupling on the order of -50 cm^{-1} . Finally, we show the frequency distribution for the fully (including intramolecular) coupled system, which shows peaks at about 3120 , 3220 , 3340 , and 3400 cm^{-1} , similar to four of the five peaks for the two partially coupled situations, but interestingly, does not show the peak at about 3260 that one might expect from both the uncoupled and strong intermolecular coupling distributions!

The fully coupled frequency distribution and various spectra are, of course, not the same because the latter involve the transition dipoles or polarizabilities, and since they have vector or tensor properties, respectively, they can interfere in complex ways. Still, it is intriguing that four of the five peaks that appear in the IR and Raman spectra (see Fig. 8), albeit with differing intensities, are essentially the same as those in the frequency distribution (to illustrate this, the same five vertical dashed lines are shown in Fig. 11). To understand the origin of the fifth and lowest-frequency (3060 cm^{-1}) peak, especially prominent in the polarized Raman spectrum, we consider the hypothetical situation where $a_{ipq} = 1$.^{47,51} This corresponds to an in-phase exciton and the hypothetical spectrum for this situation at 1 K is compared to the theoretical Raman spectrum for the aa polarization in Fig. 12. The agreement of the peak positions at about 3060 cm^{-1} demonstrates that the origin of this low-frequency peak does indeed arise from the in-phase exciton, as suggested previously.^{18,19}

Taking into account the roughly 25 cm^{-1} blue shift in going from 1 to 125 K, and an additional 40 cm^{-1} blue shift

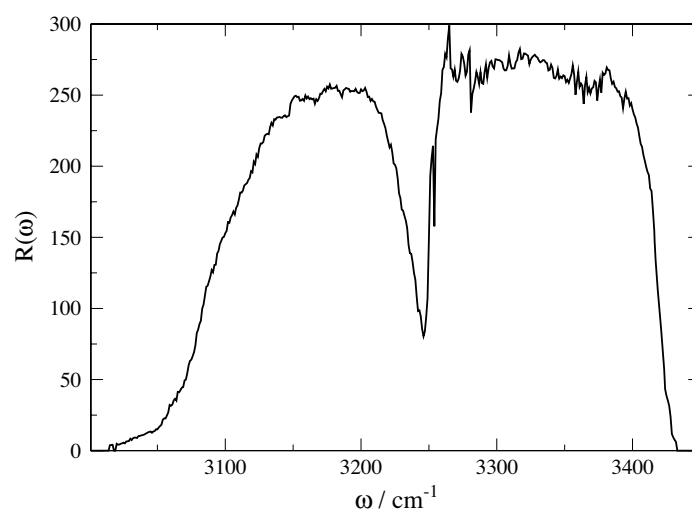


FIG. 13. Inverse participation ratio vs eigenfrequency for ice Ih at 1 K.

in going from 125 to 245 K ,³⁷ we can now assign the origin of the peaks in the experimental IR spectrum at 100 K (see Fig. 6) as due to (from left to right) strong intermolecular coupling, weak intermolecular coupling, and weak intermolecular coupling. Similarly, we can assign the origin of the peaks in the experimental Raman spectra at 269 K (see Fig. 7); they are due to (from left to right) the in-phase exciton band, weak intermolecular coupling, and strong intermolecular coupling. Presumably the same assignments also hold for the D_2O spectra (which, however, are somewhat different from the H_2O spectra, due to a different subtle interplay between coupling and disorder). These assignments are in contrast to most previous interpretations of ice Ih vibrational spectra, which invoked the symmetric and antisymmetric stretch modes of the water molecule¹⁹ or the modes of a tetrahedron of OH bonds.³⁵ As noted above, we find that in ice the intramolecular coupling is very weak, and therefore, the presence of substantial diagonal disorder makes the molecular normal modes an inappropriate basis set and not relevant for spectral assignments.

As mentioned above, in an ordered crystal at low temperature, the vibrational eigenstates would be delocalized over the entire crystal. For a disordered crystal like ice Ih, however, the situation is quite complicated. Recall that Fig. 11 shows the distribution of frequencies of the uncoupled chromophores; its width of about 70 cm^{-1} reflects the “diagonal disorder” for the exciton Hamiltonian. The dominant coupling from the strong nearest-neighbor interactions is about -50 cm^{-1} . Considering the ratio of these two, studies of Anderson localization^{70–74} would imply that the eigenstates would be delocalized. However, this does not take into account the disorder in the couplings coming from the topological proton disorder. Thus, while each OH bond is strongly coupled to four others, with an interaction of roughly -50 cm^{-1} , because of the proton disorder the pattern of the coupling is quite random. Therefore, it is not clear if the states are extended or not. To this end, we calculate the inverse participation ratio for each eigenstate and bin them up by eigenfrequency.⁴⁷ The result is shown in Fig. 13. One

sees that the typical eigenstate is extended over roughly 250 chromophores (which should be compared to about 12 in liquid water⁴⁷), out of 864. The value of the inverse participation ratio drops at about 3250 cm^{-1} because the frequency distribution also drops considerably (see Fig. 11) at this frequency, and so there are fewer near-resonant chromophores to couple to. To understand if the states are localized in the Anderson sense, we have repeated the calculation for another ice Ih lattice with 1528 chromophores.⁶⁸ The inverse participation ratio of the typical eigenstate here is about 440, significantly larger than for the original lattice, suggesting that the states are extended.

To be more quantitative, we do a crude finite-size scaling calculation by considering the “quantum connectedness length,”⁷⁴ which is one way to define a localization length, and is related to the extent to which two sites are connected through mutual overlap with eigenstates. In a finite-size scaling calculation, one compares the reduced dimensionless localization length (in this case, the localization length divided by the cube root of the unit-cell volume) for two different system sizes. If the reduced localization length is smaller for the larger system, all states are localized, while if this length is larger for the larger system, at least some states are extended.⁷⁴ We find that for the original lattice the localization length is 12.0 \AA , while for the larger lattice it is 14.5 \AA . For the reduced localization length, we obtain 0.498 for the original lattice and 0.497 for the larger lattice. The similarity of these two numbers suggests that one is close to the localization transition, and so if the states are extended, they are just so.

V. CONCLUSIONS

We have extended our calculations³⁷ of the vibrational spectroscopy of dilute HOD in H_2O and D_2O ice Ih to the case of the neat ices. Such calculations are much more difficult due to intramolecular and intermolecular vibrational couplings. To proceed within the context of our mixed quantum/classical model, we need coupling maps to supplement our previously derived transition frequency and dipole maps.³⁷ While such coupling maps have been previously developed for SPC/E water and applied to the IR and Raman spectroscopy of liquid H_2O and D_2O ,^{47,51} herein we had to develop new maps, since we were using a new and different simulation model⁴⁹ (one that freezes closer to the experimental freezing point). We calculate IR line shapes for polycrystalline Ih and Raman line shapes (all polarizations) for single crystal ice Ih, for both water and heavy water, at 1, 125, and 245 K. Where possible we compare with experiment, finding reasonable agreement. Such agreement for ice, using spectroscopic maps developed for liquid water at ambient conditions, provides evidence that the maps are transferable and can be used for other situations (supercooled water, liquid water at other temperatures, the liquid/vapor interface, supercritical water, etc.).

Our analysis of these results allows us to provide molecular and physical interpretations for several interesting phenomena. First we found that the intermolecular couplings between the nearest-neighbor local-mode chromophores are much larger than the intramolecular couplings for ice Ih

(while for water, the magnitudes are comparable⁴⁷). Both strong and weak intermolecular couplings produce new peaks in the vibrational density of states, which appear to greater or lesser extents in the different IR and Raman spectra. In addition, a collective low-frequency peak appears in the polarized Raman spectra. Because the intramolecular coupling is weaker than the diagonal disorder, interpretation of the spectra in terms of the molecular symmetric and antisymmetric normal modes is inappropriate.

The nature of the vibrational excitons at low temperature results from a competition between intermolecular coupling, which tends to delocalize the states, and diagonal and off-diagonal disorder, both of which arise from the proton disorder in ice Ih, which tend to localize the states. Our analysis shows that the states are delocalized over many chromophores and appear to be just extended in the Anderson sense. Thermal disorder at higher temperatures, which produce more diagonal disorder in the exciton Hamiltonian and would tend to further localize states, produces additional broadening in the vibrational spectra.

One exciting prospect of this work is that using the same exciton Hamiltonian and within the same framework we can calculate the anisotropy decay^{75,76} for $\text{H}_2\text{O}/\text{D}_2\text{O}$ ice mixtures, as measured recently by Timmer and Bakker²⁸ and can perhaps help interpret their results. In addition, our work can be extended to calculate vibrational spectra for other phases of ice.¹ Such calculations may help us understand the structure and dynamics of these other phases. Finally, we can extend our work on vibrational sum-frequency spectroscopy of the liquid water surface,^{77,78} to ice surfaces, with or without the quasi-liquid layer; interpretations of such systems have been controversial. We hope that our theory and results for these systems will be sufficiently accurate to contribute meaningfully to their study.

ACKNOWLEDGMENTS

This work was supported by DOE Grant No. DE-FG02-09ER16110 and NSF Grant Nos. CHE-0750307 and CHE-1058752.

¹V. F. Petrenko and R. W. Whitworth, *Physics of Ice* (Oxford University Press, Oxford, 1999).

²C. G. Salzmann, P. G. Radaelli, A. Hallbrucker, E. Mayer, and J. L. Finney, *Science* **311**, 1758 (2006).

³Y. Takii, K. Koga, and H. Tannaka, *J. Chem. Phys.* **128**, 204501 (2008).

⁴M. de Koning and A. Antonelli, *J. Chem. Phys.* **128**, 164502 (2008).

⁵C. G. Salzmann, P. G. Radaelli, E. Mayer, and J. L. Finney, *Phys. Rev. Lett.* **103**, 105701 (2009).

⁶J.-L. Kuo, M. L. Klein, and W. F. Kuhs, *J. Chem. Phys.* **123**, 134505 (2005).

⁷D. Lu, F. Gygi, and G. Galli, *Phys. Rev. Lett.* **100**, 147601 (2008).

⁸L. E. Bove, S. Klotz, A. Paciaroni, and F. Sacchetti, *Phys. Rev. Lett.* **103**, 165901 (2009).

⁹D. van der Spoel, F. R. N. C. Maia, and C. Caleman, *Phys. Chem. Chem. Phys.* **10**, 6344 (2008).

¹⁰C. Caleman and D. van der Spoel, *Angew. Chem., Int. Ed. Engl.* **47**, 1417 (2008).

¹¹C. Vega, M. Martin-Conde, and A. Patrykiewicz, *Mol. Phys.* **104**, 3583 (2006).

¹²R. G. Fernández, J. L. F. Abascal, and C. Vega, *J. Chem. Phys.* **124**, 144506 (2006).

¹³H. Bakker and J. L. Skinner, *Chem. Rev.* **110**, 1498 (2010).

- ¹⁴C. Haas and D. F. Hornig, *J. Chem. Phys.* **32**, 1763 (1960).
- ¹⁵J. E. Bertie and E. Whalley, *J. Chem. Phys.* **40**, 1638 (1964).
- ¹⁶T. Ford and M. Falk, *Can. J. Chem.* **46**, 3579 (1968).
- ¹⁷J. E. Bertie, H. J. Labbé, and E. Whalley, *J. Chem. Phys.* **50**, 4501 (1969).
- ¹⁸P. Wong and E. Whalley, *J. Chem. Phys.* **62**, 2418 (1975).
- ¹⁹E. Whalley, *Can. J. Chem.* **55**, 3429 (1977).
- ²⁰J. G. Scherer and R. G. Snyder, *J. Chem. Phys.* **67**, 4794 (1977).
- ²¹R. McGraw, W. G. Madden, S. A. Rice, and M. G. Sceats, *Chem. Phys. Lett.* **48**, 219 (1977).
- ²²T. C. Sivakumar, S. A. Rice, and M. G. Sceats, *J. Chem. Phys.* **69**, 3468 (1978).
- ²³M. S. Bergren, D. Schuh, M. G. Sceats, and S. A. Rice, *J. Chem. Phys.* **69**, 3477 (1978).
- ²⁴J. P. Devlin, *J. Chem. Phys.* **90**, 1322 (1989).
- ²⁵A. F. Goncharov, V. V. Struzhkin, H. Mao, and R. J. Hemley, *Phys. Rev. Lett.* **83**, 1998 (1999).
- ²⁶H. Iglev, M. Schmeisser, K. Simeonidas, A. Thaller, and A. Laubereau, *Nature* **439**, 183 (2006).
- ²⁷M. Schmeisser, H. Iglev, and A. Laubereau, *Chem. Phys. Lett.* **442**, 171 (2007).
- ²⁸R. L. A. Timmer and H. J. Bakker, *J. Phys. Chem. A* **114**, 4148 (2010).
- ²⁹D. Eisenberg and W. Kauzmann, *The Structure and Properties of Water* (Oxford University Press, New York, 1969).
- ³⁰*Water: A Comprehensive Treatise*, edited by F. Franks (Plenum, New York, 1972), Vol. 1.
- ³¹R. McGraw, W. Madden, M. Bergren, and S. Rice, *J. Chem. Phys.* **69**, 3483 (1978).
- ³²M. S. Bergren and S. A. Rice, *J. Chem. Phys.* **77**, 583 (1982).
- ³³S. Rice, M. Bergren, A. Belch, and N. Nielson, *J. Phys. Chem.* **87**, 4295 (1983).
- ³⁴M. Wojcik, V. Buch, and J. Devlin, *J. Chem. Phys.* **99**, 2332 (1993).
- ³⁵V. Buch and J. P. Devlin, *J. Chem. Phys.* **110**, 3437 (1999).
- ³⁶M. J. Wójcik, K. Szczeponek, and S. Ikeda, *J. Chem. Phys.* **117**, 9850 (2002).
- ³⁷F. Li and J. L. Skinner, *J. Chem. Phys.* **132**, 204505 (2010).
- ³⁸C. Lee, D. Vanderbilt, K. Laasonen, R. Car, and M. Parrinello, *Phys. Rev. B* **47**, 4863 (1993).
- ³⁹J. Li, *J. Phys. Chem. B* **101**, 6237 (1997).
- ⁴⁰C. J. Burnham, J.-C. Li, and M. Leslie, *J. Phys. Chem. B* **101**, 6192 (1997).
- ⁴¹A. Putrino and M. Parrinello, *Phys. Rev. Lett.* **88**, 176401 (2002).
- ⁴²R. Iftimie and M. E. Tuckerman, *J. Chem. Phys.* **122**, 214508 (2005).
- ⁴³W. Chen, M. Sharma, R. Resta, G. Galli, and R. Car, *Phys. Rev. B* **77**, 245114 (2008).
- ⁴⁴S. A. Corcelli, C. P. Lawrence, and J. L. Skinner, *J. Chem. Phys.* **120**, 8107 (2004).
- ⁴⁵B. Auer, R. Kumar, J. R. Schmidt, and J. L. Skinner, *Proc. Natl. Acad. Sci. U.S.A.* **104**, 14215 (2007).
- ⁴⁶J. R. Schmidt, S. T. Roberts, J. J. Loparo, A. Tokmakoff, M. D. Fayer, and J. L. Skinner, *Chem. Phys.* **341**, 143 (2007).
- ⁴⁷B. M. Auer and J. L. Skinner, *J. Chem. Phys.* **128**, 224511 (2008).
- ⁴⁸J. L. Skinner, B. M. Auer, and Y.-S. Lin, *Adv. Chem. Phys.* **142**, 59 (2009).
- ⁴⁹R. Kumar and J. L. Skinner, *J. Phys. Chem. B* **112**, 8311 (2008).
- ⁵⁰W. L. Jorgensen, J. Chandrasekhar, J. D. Madura, R. W. Impey, and M. L. Klein, *J. Chem. Phys.* **79**, 926 (1983).
- ⁵¹M. Yang and J. L. Skinner, *Phys. Chem. Chem. Phys.* **12**, 982 (2010).
- ⁵²D. A. McQuarrie, *Statistical Mechanics* (Harper and Row, New York, 1976).
- ⁵³E. B. Wilson, J. C. Decius, and P. C. Cross, *Molecular Vibrations* (Dover, New York, 1980).
- ⁵⁴D. Colbert and W. H. Miller, *J. Chem. Phys.* **96**, 1982 (1992).
- ⁵⁵N. Balakrishnan, C. Kalyanaraman, and N. Sathymurthy, *Phys. Rep.* **280**, 79 (1997).
- ⁵⁶W. S. Benedict, N. Gailar, and E. K. Plyler, *J. Chem. Phys.* **21**, 1301 (1953).
- ⁵⁷M. S. Child and T. R. Lawton, *Chem. Phys. Lett.* **87**, 217 (1982).
- ⁵⁸V. Buch, *J. Phys. Chem. B* **109**, 17771 (2005).
- ⁵⁹H. Torii, *J. Phys. Chem. A* **110**, 4822 (2006).
- ⁶⁰D. van der Spoel, E. Lindahl, B. Hess, A. R. van Buuren, E. Apol, P. J. Meulenhoff, D. P. Tieleman, A. L. T. M. Sijbers, K. A. Feenstra, R. van Drunen, and H. J. C. Berendsen, *GROMACS User Manual version 3.3* (www.gromacs.org, 2005).
- ⁶¹T. Darden, D. York, and L. Pedersen, *J. Chem. Phys.* **98**, 10089 (1993).
- ⁶²U. Essmann, L. Perera, M. L. Berkowitz, T. Darden, H. Lee, and L. G. Pedersen, *J. Chem. Phys.* **103**, 8577 (1995).
- ⁶³S. Miyamoto and P. A. Kollman, *J. Comput. Chem.* **13**, 952 (1992).
- ⁶⁴A. J. Lock and H. J. Bakker, *J. Chem. Phys.* **117**, 1708 (2002).
- ⁶⁵J. E. Bertie and Z. Lan, *Appl. Spectrosc.* **50**, 1047 (1996).
- ⁶⁶J. R. Scherer, M. K. Go, and S. Kint, *J. Phys. Chem.* **78**, 1304 (1974).
- ⁶⁷J.-J. Max and C. Chapados, *J. Chem. Phys.* **131**, 184505 (2009).
- ⁶⁸J. Hayward and J. Reimers, *J. Chem. Phys.* **106**, 1518 (1997).
- ⁶⁹J. R. Schmidt, S. A. Corcelli, and J. L. Skinner, *J. Chem. Phys.* **123**, 044513 (2005).
- ⁷⁰P. W. Anderson, *Phys. Rev.* **109**, 1492 (1958).
- ⁷¹A. MacKinnon and B. Kramer, *Z. Phys. B* **53**, 1 (1983).
- ⁷²B. R. Bulka, B. Kramer, and A. MacKinnon, *Z. Phys. B* **60**, 13 (1985).
- ⁷³B. Bulka, M. Schreiber, and B. Kramer, *Z. Phys. B* **66**, 21 (1987).
- ⁷⁴J. L. Skinner, *J. Phys. Chem.* **98**, 2503 (1994).
- ⁷⁵Y.-S. Lin, P. A. Pieniazek, M. Yang, and J. L. Skinner, *J. Chem. Phys.* **132**, 174505 (2010).
- ⁷⁶T. I. C. Jansen, B. M. Auer, M. Yang, and J. L. Skinner, *J. Chem. Phys.* **132**, 224503 (2010).
- ⁷⁷B. Auer and J. L. Skinner, *J. Chem. Phys.* **129**, 214705 (2008).
- ⁷⁸B. Auer and J. L. Skinner, *J. Phys. Chem. B* **113**, 4125 (2009).